Genesis Solar Wind Concentrator: Computer Simulations of Performance Under Solar Wind Conditions

Roger C. Wiens[1]

Marcia Neugebauer[2]

Daniel B. Reisenfeld[1]

Ronald W. Moses, Jr.[3]

Jane E. Nordholt[4]

Donald S. Burnett[5]

[1]Space & Atmospheric Sciences, NIS-1, MS D466, Los Alamos National Laboratory, Los Alamos, NM 87545; rwiens@lanl.gov

[2]Jet Propulsion Laboratory, MS 169-506, 4800 Oak Grove Drive, Pasadena, CA 91109

[3]Theoretical Division, T-3, MS B216, Los Alamos National Laboratory

[4]P-21, MS D454, Los Alamos National Laboratory

[5]Geological and Planetary Sciences, MS 100-23, California Institute of Technology, 1201 E. California Boulevard, Pasadena, CA 91125

Abstract

The design and operation of the Genesis Solar-Wind Concentrator relies heavily on computer simulations. The computer model is described here, as well as the solar wind conditions used as simulation inputs, including oxygen charge state, velocity, thermal, and angular distributions. The simulation included effects such as ion backscattering losses, which also affect the mass fractionation of the instrument. Calculations were performed for oxygen, the principal element of interest, as well as for H and He. Ion fluences and oxygen mass fractionation are determined as a function of radius on the target. The results were used to verify that the instrument was indeed meeting its requirements, and will help prepare for distribution of the target samples upon return of the instrument to earth. The actual instrumental fractionation will be determined at that time by comparing solar-wind neon isotope ratios measured in passive collectors with neon in the Concentrator target, and by using a model similar to the one described here to extrapolate the instrumental fractionation to oxygen isotopes.

1. Introduction

The Solar-Wind Concentrator is designed to provide a high-fluence sample of the solar wind, particularly of elements in the mass range between 4 and ~28 amu, by focusing a large cross section of solar-wind ions onto a small target. The primary purpose of the Concentrator is to obtain a sufficient sample of solar-wind oxygen to enable a high-precision isotopic measurement in spite of the ubiquitous oxygen backgrounds in terrestrial materials. Such a measurement may reveal the cause of the oxygen isotopic heterogeneity among solar-system objects (Wiens et al., 1999). A key assumption in this endeavor is that the solar-wind isotopic composition is representative of the isotopic composition of the solar photosphere for elements heavier than helium. The Genesis mission will measure the isotopic composition of other elements, such as Ne, Mg, or Si, to unprecedented precision in three different solar-wind regimes--coronal hole, interstream, and coronal mass ejections. If the isotopic compositions of these regimes are identical, the solar wind isotopic composition will be assumed to be representative of the solar photosphere. Isotopic differences would complicate interpretations of the solar composition, though information on isotopic fractionation of heavy elements between regimes would be valuable input to solar-wind acceleration models.

The Genesis Solar-Wind Concentrator is a unique instrument in the magnitude of the concentration achieved (averaging a factor of 20x), the fidelity required in understanding its mass fractionation characteristics (instrumental fractionation needs to be known to one permil, that is, $\pm 0.1\%$, 2-σ), and in the fact that the instrument focuses ions onto a solid target to be analyzed on the ground after the spacecraft returns, rather than having an active detector. Most solar-wind instruments to date have relatively small apertures, usually well under 1 cm^2, with the largest around 100 cm^2. These instruments can be tested using narrow ion beams that are easily produced in the laboratory. By contrast, the Genesis Concentrator has an aperture of nearly 1300 cm^2. It is practically impossible to reasonably simulate the solar wind with an ion beam covering such a large area. The CASYMS system at the University of Bern comes the closest, as it has a ~0.6 m. diameter plasma beam (Ghielmetti et al., 1983). However, the uniformity of this

beam over the 40 cm diameter aperture of the Concentrator is not sufficient to accurately characterize the Concentrator optics to the desired degree. Secondly, the charge states obtainable in plasma test chambers only approach those in the solar wind if an electron cyclotron resonance (ECR) ion source is used, and no such sources are available in tandem with a wide beam. Even with high charge state capabilities, the distribution of charge states, angles, and velocities cannot be duplicated together. Finally, even if a large, high fidelity solar wind-like beam were to be achieved, verification of the Concentrator optics would be very time-consuming because each target analysis is a lengthy process using mass spectrometry, e.g., secondary ion mass spectrometry, and requiring significant isotopic calibration.

For these reasons it was decided to test the solar-wind-condition performance of the Concentrator by using an ion simulation code after verifying that the code gave results predicted by laboratory ion beam conditions. Laboratory validation of the simulations is described in the companion paper on the Concentrator design (Nordholt *et al.*, 2002). Here we describe the Concentrator model and solar-wind conditions used in the simulation code, and give the results of the simulations. Concentrator components mentioned here are defined and illustrated in Nordholt *et al.* (2002), which may be needed for cross-reference. Following a description of the computer model in the next section of this paper, the various solar wind parameters used in the tests are described in Section 3. Specific interactions between the instrument and the solar wind are described in Section 4. Finally, the results, in terms of ion patterns on the target, are given and discussed in Section 5.

While the simulations described here predict that the Concentrator will give the desired performance, these simulations are clearly not the last word on Concentrator performance. Solar-wind oxygen compositions determined from Concentrator samples will rely on corrections for instrumental (e.g., Concentrator) fractionation based on comparison of solar-wind neon isotopic compositions measured in passive collectors with neon isotopic compositions in the Concentrator target. The instrumental fractionation specific to oxygen m/q states will then be determined by re-running the simulations described here for both oxygen and neon under the actual conditions encountered and archived during the Genesis collection period. This will require a good understanding of charge state conditions during this time period, obtainable from other spacecraft instruments such as ACE SWICS.

The simulations described below focus on determining mass fractionation based on mass per charge (m/q) rather than the more familiar energy per charge (E/q) because of the way the Concentrator is operated in space. Because it is impossible for an electrostatic concentrator with a fixed voltage to operate with high efficiency over the large range in solar-wind energies, the Concentrator voltages are adjusted to continuously track the solar wind proton energy based on real-time data from the Genesis ion monitor (Barraclough et al., 2002). By continuously adjusting the voltages, the energy dependence is removed to zeroth order, leaving a dependence on m/q. There are still performance variations as a function of velocity, so mass fractionation estimates are obtained by using reasonable charge state distributions for the solar wind at different velocities, as described in detail below.

2. Concentrator Simulation Model

SIMION 7.0 (D.A. Dahl, Bechtel Idaho) was chosen for Concentrator modeling. While there exist a number of ion-trajectory programs, they tend to be written with electrostatic or magnetic sector spectrometers in mind. Their geometries are quite specific and very different from the Concentrator, with its large field regions. SIMION is sufficiently general that the Concentrator could be successfully modeled. SIMION employs 3-dimensional arrays of points in space over which it solves the Laplace equation. It then "flies" ions through these arrays, recording their impact positions on solid surfaces.

The simulation model incorporates nearly all of the components used in the actual instrument. The model is shown in Fig. 1. Briefly, the major ion optical elements are, in the order encountered by the ions, a grounded grid across the aperture, followed by a proton rejection grid, which is positively biased to reject >90% of the protons, minimizing ion radiation damage at the target. The voltage of the grid is adjusted continuously in flight to levels relative to the peak of the real-time proton energy distributions (E_p), as will be described in more detail below. The third optical element is the acceleration grid, which is biased at –6.5 kV to accelerate the remaining ions, thereby straightening their trajectories and providing more energy for deeper implantation in the target. After the acceleration grid, the ions pass through a field-free region bounded on the other end by a parabolic domed grid. The mirror electrode is positively biased, again based on real-time solar wind energy data as described below. Although parabolic in overall shape, the curvature actually consists of 0.1 mm steps so as to act on photons as a reverse Fresnel lens to avoid focusing sunlight on the target, heating it excessively. The ions are reflected by parabolically shaped equipotentials between the domed grid and mirror electrode. The ions pass back through the domed grid and are focused on the target.

The simulation model was limited by software and memory to less than fifty million array points. Achieving the maximum resolution within this limitation required economizing array points by using symmetry and by eliminating portions of the model that were not necessary. Near the flat grids and the mirror electrode (Fig. 1), the geometry of the outer housing has a significant influence on the trajectories of ions near the edge, so the ion optic model must extend all the way out to ~23 cm radius. If the housing cutout for the high voltage bus bar is ignored (a 2.5 cm diameter hole in the housing that is level with the lip of the mirror electrode; cf. Fig. 18 of Nordholt et al., 2002), advantage can be taken of two axes of symmetry, so that the model need only cover one quarter of the Concentrator. Additionally, the region between the accelerator grid and the domed grid is field free, and therefore needs not be modeled with array points. To take advantage of this field-free region in the center of the instrument, the model is broken into two "instances", or portions containing array points. As shown in Fig. 1, instance 1 contains the flat grids and target; instance 2 contains the domed grid and mirror electrode. Ion trajectories start inside of instance 1 just above the ground grid. Once the ions leave instance 1 they coast with no forces acting on them until they enter instance 2 or leave the simulated region. Because the portion in between instances is not modeled, the Accelerator Can, which is the inner wall of the Concentrator in the field-free region, is missing from the simulation model. Most of the ions that would normally strike the Accelerator Can walls are lost from the simulation by exiting between the instances. A few of the ions that would normally strike the Accelerator Can end up outside of the Accelerator Can radius but inside the radius of the grounded housing. To keep these from re-entering the simulation model between the Accelerator Can and the housing, which is physically impossible in the actual Concentrator, a series of narrow rings, providing the

desired voltage gradient, were added to the simulation model in this region (Fig. 1). The channels between rings of different voltages are too narrow and long to allow ions to pass. The rings have no effect on ions flying in the main portion of the Concentrator.

For this design, the limitations on total array points allow for a maximum array point spacing of 1.5 per mm. The upper instance has 5.3 million points, and the lower instance has 17.7 million points. It would be possible to decrease the array point spacing by a few percent with some loss in computing speed, however an array point spacing of 2.0 per mm would result in over fifty million points, the maximum allowed by the program. The 0.67 mm resolution in the set-up described above is somewhat coarse, but still sufficient for modeling the Concentrator performance as long as certain exceptions are taken into account. In particular, the high transparency grids can only be modeled as smooth membranes rather than individual grid wires. At 0.025 mm, the diameter of the grid wires is far smaller than the model resolution. The generally slight scattering of ions due to passage close to grid wires is therefore treated separately, as described in Section 4.2. Secondly, the mirror electrode microstepping is at 0.1 mm intervals, only a few times smaller than the computer model steps. This difference does not present a problem within the normal range of ion energies input to the Concentrator, for which ions remain much further from the surface.

SIMION does not directly model voltage gradients across insulators. However, in the Concentrator design the insulators are too near the active regions to be ignored. The insulators were therefore modeled as a series of equipotential bars perpendicular to the voltage gradient, as shown in Fig. 1. This is certainly reasonable for the slightly-conductive coated insulators supporting the mirror electrode, and should be reasonable for the other insulators, which are uncoated alumina (Nordholt et al., 2002).

3.   Solar Wind Parameters

The parameters of the solar wind ions input into the model are critical to obtaining realistic results. This section describes these parameters. The ones considered here are charge state, bulk velocity, angle, and thermal Mach number. For some parameters, namely charge state and angular distribution, the same values were used for nearly all runs, based on grand averages of several years of solar wind data. For bulk flow velocity a number of runs were executed to cover the range of solar wind speeds. For all runs a Monte Carlo spatial distribution was used covering a circular area extending to a radius of 20.8 cm, slightly larger than the 20.6 cm radius of the ground grid, with ions started 1 mm above the grid.

3.1   Charge State Distribution. For oxygen, only charge states +5 to +8 were considered, as lower charge states of actual solar wind constitute well under 1% at all velocities (Wimmer-Schweingruber *et al.*, 1998; Geiss *et al.*, 1992). The charge state distribution used for modeling is given in Table 1. Initial modeling used the low-speed solar wind distributions given in Geiss et al. (1992). Final calculations used oxygen 7/6 charge state ratios from ACE SWICS data taken between February 6, 1998 and July 1, 2000 for solar wind < 700 km/s. For 700-800 km/s, where ACE statistics are poor, Ulysses SWICS data were used. Distributions of the minor ions +5 and +8 were then calculated for the given 7/6 ratio based on equilibrium thermal models (Summers, 1972; Nahar, 1999).

The ion energy per charge (E/q) ratio strongly affects the degree to which ion trajectories are straightened by the acceleration grid and the depth of penetration of the ion into the region between the domed grid and the mirror electrode for a given Concentrator voltage setting. For a given isotope, adjusting the mirror voltage as a function of E_p largely compensates the energy factor at the mirror (Nordholt et al., 2002). That leaves the charge state, q, as the main factor in the mirror. The simulations assume there is no isotopic mass bias as a function of q in the solar wind.

3.2 Velocity Distribution. The overall performance of the Concentrator is affected by the long-term average energy or velocity distribution (the discussion here will use velocity rather than energy). Unfortunately, because Concentrator voltages are adjusted based on real-time proton velocity, separate runs must be made with different voltage settings for each bulk velocity modeled. Initial runs focused mostly on optimizing the Concentrator design for medium-speed solar wind conditions (e.g., 1 keV/amu, or 440 km/s), with some attention paid to extremes (300 and 800 km/s). A final set of runs was done for $^{16,18}O$, He, and H, spanning the range of velocities, run at 100 km/s intervals between 350 and 750 km/s. The results of these runs were combined based on the weighting of the velocity distribution shown in Fig. 2, which were taken from hourly averages in NASA's OMNI data file. Modeling of heavy ions using proton velocities ignores the observed slight velocity differences between protons and heavier ions. This velocity difference varies between ~0 for low-speed wind and ~50 km/s for high speed wind.

3.3 Angular Distribution. The net ion angular distribution results from a number of different effects, including ion thermal distribution, bulk flow angle, spacecraft and solar wind relative velocities, spacecraft spin axis, wobble and nutation, and the instrument alignment. The overall expected angular distribution is shown in Fig. 3. It is assumed that all ion species have the same thermal speed and the same distribution of bulk flow directions. Instrument alignment is within 1 degree of the spacecraft spin axis, which can be ignored. To account for spacecraft velocity around the sun, the spacecraft is pointed 4.5 degrees ahead of the sun on average. Daily precession maneuvers, along with limitations on spacecraft wobble and nutation, are intended to keep the spacecraft within 2 degrees of its nominal pointing. The model assumes the spacecraft is on average 2 degrees off of nominal pointing. Minimizing wobble and nutation is more difficult on the Genesis spacecraft due to the movement of collector arrays. Analysis of the effect of spacecraft pointing indicates that there is very little difference in the angular distribution for higher accuracy spacecraft pointing, but the angular distribution starts to affect Concentrator performance above 2 degrees off nominal pointing.

3.4 Thermal distribution. Besides angular distribution, the thermal distribution causes an instantaneous spread in the velocity of incoming ions which is generally greater than the variation in bulk flow velocity over the 2.5 minute duration it takes to obtain new velocity data from GIM (Barraclough et al., 2002). The thermal Mach number distribution from the OMNI database for 1991-1992 is shown in Fig. 4. It was mostly used to determine the efficiency of the rejection grid in getting rid of protons, based on the operation philosophy described in Nordholt et al. (2002). For a given thermal Mach number, e.g.,

$$M_{th} = \sqrt{(mv^2/2kT)} = \sqrt{(E_p/kT)} \qquad [1]$$

and grid voltage setting, theoretical rejection fractions are relatively straightforwardly determined. Different thermal Mach numbers were tested in the Concentrator simulations in a limited way. A branch of the code was built in which the ions' parallel velocity fitted a thermal Mach number distribution, while the overall angular distribution remained the same. In these runs the overall concentration efficiency remained relatively unchanged over a large range of Mach numbers but the isotopic pattern on the target varied somewhat at low Mach numbers, as will be discussed later in Section 5.3. In reality, thermal Mach number variations will affect the angular distribution, which will in turn affect the overall collection efficiency. This level of complexity was not attempted in the model, as a mean angular distribution was used instead of additional individual runs.

4.   Interactions Between Concentrator and Solar Wind

In this section we discuss physical interactions which are relevant and which were determined by means other than the SIMION model. Some of these results were incorporated into the SIMION model for better fidelity. This section includes a discussion of the operation of the hydrogen rejection grid, scattering of ions by individual grid wires, and backscattering of ions from the various target materials.

4.1   Proton Rejection and Heavy Ion Fractionation by the Hydrogen Rejection Grid.   The Concentrator is designed to reject as much of the proton flux as possible without mass fractionating the heavier ions. If the solar wind were always a cold plasma it would be relatively simple to reject protons and collect the heavier species, as the E/q ratio, which for a given velocity is proportional to mass per charge (m/q), differs significantly between hydrogen, at m/q = 1.0, and all other species, at m/q $\geq$ 2.0. However, as the temperature increases the E/q of the different species overlap to an increasing degree. To avoid losing heavy ions--and fractionating them in the process--some hydrogen must be allowed to pass. Fig. 5 shows the fraction of hydrogen admitted through the rejection grid as a function of thermal Mach number for three different ratios (R) of rejection grid voltage (V_H) to the peak of the proton energy distribution, E_p:

$$V_H = E_p \times R \qquad\qquad [2]$$

Fig. 6 shows the fractionation of $^{18}O/^{16}O$ for +8 charge species. The rejection grid operation was designed so that fractionation of this species would be under 1 permil at all times. This is done by switching R values, and hence the rejection grid voltage, as a function of thermal Mach number (cf. Table 4, Nordholt et al., 2002). Because O^{+8} is usually a relatively minor charge state, except in some CME flows (T. Zurbuchen, personal communication, 2002), and is the worst case for fractionation, the average fractionation of oxygen by the H rejection grid should be < 0.1 permil.

4.2 Grid Scattering. A separate issue is the scattering of ion trajectories by passage through the grids. SIMION treats the grids as perfect membranes when in reality they are small wires with large voids between them. Electrostatic potentials poke through these voids, creating an uneven voltage "surface". The scattering occurs at all grids. However, the effect is greatest where the fields are the strongest on both sides of the grid, which is true of the rejection grid. The axially symmetric component of the grid scattering can be treated as a perturbation on the angular

distribution of the incoming ions. When this is done, it can be shown that the difference for heavy ions is minor in comparison to the actual uncertainty of other contributions to the curve in Fig. 3, such as from spacecraft pointing. But for protons, because the field perturbations near the grid wires are of the order of the proton energies near the rejection grid, the grid scattering contribution is significant. The dashed curve in Fig. 3 shows the effective angular distribution of incoming protons after the grid scattering is folded in. There is significant uncertainty associated with this model due to the fact that it is a point design for one solar wind speed and Concentrator voltage setting. This suggests that the H distribution on the target is still relatively uncertain.

The non-axisymmetric grid scattering component was shown to be strongest near the center of the target, where the concentration gradient was steepest. For heavy ions it is significant only within the inner 2-3 mm. Because the target quadrants to be analyzed do not extend within 3 mm of the center, this non-axisymmetric scattering of heavy ions is of no consequence. There may, however, be measurable differences in the H fluence as a function of radial angle on the main portion of the target.

4.3 Backscattering Losses of Ions at the Target. Backscattering of ions from a surface is a well-known phenomenon. Backscattering occurs most readily for light ions incident on high atomic mass substrates, for ions with relatively low energies, and for relatively high incidence angles from the normal. The Concentrator target materials are relatively comparable in atomic mass to the oxygen ions of interest. While backscattering is relatively low for oxygen, the ions are in a region where mass is a significant factor. In other words, the mass difference between 16 and 18 amu makes a difference in the fraction backscattered. Additionally, the angle of incidence from the mirror to the target is relatively high, up to ~60 deg. The TRIM/SRIM code (IBM) was used to estimate mass fractionation of oxygen due to backscattering as a function of target material, incidence angle, and ion energy. The Concentrator's acceleration potential ensures that ion energies are significantly higher than nominal solar wind energies. However, there is a range of energies, depending primarily on charge state. For example, a medium velocity (440 km/s) $^{16}O^{+6}$ ion will have 16 keV initial energy plus 6.5 kV x 6 = 39 keV acceleration energy for a total of 55 keV. A +5 ion in the same flow will have 48.5 keV, while a +8 ion will have 68 keV. A low-speed $^{16}O^{+5}$ ion could have as little as 40 keV. The highest energy oxygen ions will be a little over 100 keV. Approximately 1 million ions were flown in TRIM for each of ^{16}O and ^{18}O at a number of energies for both diamond and SiC, the two materials used in the Concentrator target. H and He ions were also run to check their backscattering losses.

Backscattering losses are highest for H and He due to their low atomic masses, ranging up to ~12% for He into SiC at relatively high incidence angles. The results for oxygen are shown in Fig. 7. For each data point the ^{16}O was input with the energy given, while the ^{18}O was input with 1 keV higher energy. During periods of moderate to high solar wind velocity, the energy difference between the isotopes will be greater, but the higher energy will also mean less fractionation. The fractions of ions lost by backscattering ranged from 0.07 to 1.07% for ^{16}O into diamond and from 0.64 to 4.67% for ^{16}O into SiC over the range of angles and energies in Fig. 7. To simulate backscattering in the SIMION models, the angle at which each ion struck the target was determined, and based on the angle and energy, each ion was given the appropriate probability of being backscattered.

4.4 Space Charge Effects. Because ions were flown on an individual basis, SIMION did not take into account space charge effects. Space charge effects are considered to be negligible for a number of reasons. Firstly, hydrogen, the dominant solar-wind component, is reduced by a factor of ~10 most of the time. Secondly, ions approach the target from a large range of angles rather than forming a collimated narrow beam. Thirdly, the ions are accelerated so that they transit any high-charge-density regions rapidly. The result is that under worst case conditions space charge effects make no more than a few nm difference in the final position of an ion on the target.

5.   Ion Collection Patterns on the Target.

After the design was finalized and the various aspects described above were thoroughly studied, a final set of runs was made taking into account angular distribution (with azimuthally averaged grid scattering folded in), charge state distributions, and backscattering. As mentioned above, separate runs had to be made to cover different velocity ranges, as the voltages must be adjusted between each run. Runs of up to 2 million ions were carried out for each velocity, ion, and target material, with over 20 million ions run in total. The output was a distribution of radial positions on the target for ions that were not backscattered. These were tabulated by 5 mm radial bins to allow sufficient statistics in each bin.

5.1 Concentration Factor and Collection Efficiency. The total fraction of ions hitting the target gives the average concentration once grid transparency, the geometric aperture to target ratio, and a correction for the actual aperture of the instrument are factored in. The latter factor is necessary because the radius over which ions were started, 20.8 cm, was slightly larger than the grid apertures, 20.6 cm at the ground grid and 20.0 cm at the domed grid, to allow ions to enter at an angle. Because of greater backscattering losses for the SiC portion of the target, the average concentration factor differs slightly between diamond and SiC, at 20.9 and 21.2, respectively. These concentration factors are relative to the total fluence of ions, not relative to passive collectors, for which backscatter losses would need to be considered. Concentration factors relative to passive collectors would thus be slightly higher. The fraction of ions that pass the grid structure but miss the target is relatively low, averaging slightly less than 10%. This fraction is particularly low for low-speed solar wind, where the Concentrator is more efficient due to the increased efficiency of the acceleration voltage in straightening the incoming trajectories of lower-speed ions. For example, the fraction missing the target at 350 km/s is < 2%. By 650 km/s almost 30% of the ions heading toward the target miss it. A change takes place in the Concentrator operation at 666 km/s, where the maximum mirror potential of 10 kV is reached. Consequently, ions of higher velocity reflect deeper in the mirror gap, which tends to focus them more efficiently. This plays against the decreasing effectiveness of the acceleration voltage at straightening the trajectories, resulting in approximately the same collection efficiency at 750 km/s as at 650 km/s.

A result of the more efficient focusing of low-speed ions is that the center of the target predominantly samples low-speed solar wind, while the outer portion disproportionately represents high-speed wind. This is seen in Fig. 8, where the relative fractions of solar wind in a given velocity range are shown for various radial distances from the center of the target. The < 400 km/s wind has dropped at the outer edge to approximately half its relative contribution at the

center. In terms of relative contribution, the high-speed solar wind increases out to the edge in Fig. 8. However, in absolute terms these fluences drop from the center to the edge as well, because the total ion fluence is relatively sharply peaked at the center of the target, as discussed below.

5.2. Concentration and Ion Fluence Patterns. Fig. 9 shows the concentration factor as a function of target radius for ^{16}O, ^{4}He^{+2}, and H. The data points represent 5 mm radial averages. The curve is a smoothed fit to the data points. Error bars show the 1-sigma statistical uncertainties. The gradient from the center reflects, to some degree, the angular distribution of incoming solar wind ions. Ions entering at a larger angle tend to strike the target at a higher radius. However, the Concentrator does not 'image' perfectly. This is because the domed grid has significant deviations from the ideal parabolic shape built in that intentionally blur the image (Nordholt et al., 2002). This blurring lowers the concentration gradient by spreading ions further from the center of the target. [As is described below and in Nordholt et al. (2002), this blurring is desirable because it reduces the mass fractionation gradient between the center and outer edge of the target.] The He concentration-factor curve in Fig. 9 is nearly identical to that of oxygen. Helium has a mass/charge ratio of 2.0, while the majority of ^{16}O is at 2.67, with a range from 2.0 to 3.2. The similarity of these curves shows the relative insensitivity on this scale to differences in the mass/charge ratio. This is of course necessary to minimize isotopic mass fractionation, which will be discussed below. The calculated He and H concentration factors do not include backscattering losses, which would lower the expected fluences by a few percent each. The proton pattern is quite highly uncertain due to the strong interactions with the rejection grid, as mentioned in Section 4.2. The proton pattern was produced by using a thermal Mach number of 8, with the rejection grid set at a voltage to proton energy ratio, R, of 1.1 (e.g., Table 4 in Nordholt et al., 2002). This is the R and Mach number combination giving the largest contribution of protons, based on the Mach number frequency curves and the relative efficiency of rejection at each Mach number. The proton concentration curve was built up by the weighted contributions at various velocities, similar to the oxygen and helium calculations.

Fig. 10 shows the expected ion density patterns on the target for ^{16}O, ^{4}He, and H, based on two years of operation. The mission's collection time may be slightly longer, raising all curves by up to 20%. Assuming 2 years of collection, the maximum oxygen fluence in the analyzable portion of the target (e.g., r > 5 mm) is 5 x 10^{14} cm^{-2}, or 13 ng/cm^2. Maximum helium and hydrogen fluences on this part of the target are 4 x 10^{16} and 6 x 10^{16} cm^{-2}, respectively, and drop off with increasing radius similar to oxygen. Radiation damage to the target from both protons and alpha particles is a potential concern. It is not possible to reject helium because its m/q ratio is in the same range as oxygen. At 4 x 10^{16} cm^{-2}, alpha particles are below the threshold at which damage begins to occur. Hydrogen is likely to diffuse out of SiC. As the primary radiation damage comes from blistering due to gas bubble formation within the substrate where the influx overwhelms diffusive losses, the relatively rapid diffusion of hydrogen out of SiC mostly eliminates proton radiation damage concerns there. Hydrogen is likely to be retentively held in diamond. However, the calculated proton fluence is below the threshold at which radiation damage is observed. Tests performed on diamond substrates confirmed that implanted oxygen is retentively held after a hydrogen fluence of 1×10^{17} cm^{-2} at the energies expected for ions impacting the Concentrator target.

5.3   Oxygen Isotopic Fractionation. ^{16}O and ^{18}O ions were flown using the same velocity and angular distributions.   The two isotopes interact differently with the Concentrator voltages because of their different energies, and they have different backscattering fractions at the target surface.   The 'instrumental' fractionation for the Concentrator, averaged over the target, is −0.39±0.43 permil per amu for SiC targets and −1.61±0.38 for diamond, where the uncertainty is based on 1-sigma statistics. (Alternately, the fractionation factor, α = 0.999615±0.00043 and 0.99839±0.00038 per amu for SiC and diamond, respectively.) The difference between the two targets is solely due to backscattering. As with the overall concentration, the mass fractionation pattern varies with radius on the target, and also with velocity. In fact, because it was optimized for the mean solar wind energy of ~1 keV/amu (440 km/s), the high-speed solar wind has relatively large variations in fractionation factor as a function of radius.   The fractionation patterns on the target are shown for different velocity bins in Fig. 11. The <400 km/s velocity bin, which comprises more than 40% of the ecliptic solar wind, is essentially flat within uncertainty over the inner four radius bins. Near the outer edge of the target, the fractionation factor rises. The acceleration grid is more efficient at focusing ^{16}O than ^{17}O or ^{18}O with their slightly higher initial energies. With a perfectly parabolic domed grid, the overall pattern would thus go from isotopically light in the center, where more ^{16}O is focused, to heavy near the edges, where the fringes of the heavy isotopes protrude past the edge of the ^{16}O pattern.

The deviations from the ideal parabolic shape in the domed grid (Nordholt et al., 2002) counteract this tendency towards light isotope enrichment in the center. The light isotopes are more strongly affected by these deviations in the domed grid because, with their lower energy, they reflect closer to the grid. With a perfectly parabolic domed grid, all ions would be sharply focused near the center of the target. The domed grid deviations from a parabola serve to smear ions away from the center. This smearing effect is stronger for ^{16}O, leaving a heavy isotope enrichment near the center. This tendency is particularly obvious for higher velocity ions for two reasons. One is that the relative effect of the acceleration grid is diminished for ions with higher incoming energy. The second reason is that penetration depth into the gap between the domed grid and the mirror electrode decreases at higher solar wind energies. The closer the ions reflect to the domed grid, the greater is the effect of the domed grid deviations from parabolic. The penetration depth decreases at high velocities because the spread in penetration depth between various charge states increases.

A slight digression into the operation of the mirror is necessary to explain this point.   As described in Nordholt *et al.*, (2002), the mirror voltage is maintained at 4.32 x E_p for all but the highest velocity solar wind. The value of 4.32 is required to keep a margin of 20% in energy on the highest expected m/q for oxygen of 18/5. That is, a ^{18}O^{+5} ion with energy 20% above the nominal for that proton velocity would just touch the mirror electrode if the ion were normally incident and the mirror were flat. The relative penetration depth of a normally-incident ion of mass *m* in amu, energy *E* in eV and charge *q*, in an ideal flat mirror is easily calculated from
$$d/D = (V_{accel} + E/q) / (V_{accel} + V_{mirror}) = (V_{accel} + mE_p/q) / (V_{accel} + 4.32E_p) \qquad [3]$$
where V_{accel} and V_{mirror} are acceleration and mirror voltages, respectively. Table 2 gives d/D ratios for ^{16}O at different charge states and velocities for a flat mirror. The results show that the penetration depths decrease with increasing ion velocity. This occurs until the maximum mirror potential of 10 kV is reached at 666 km/s. Above this, the penetration depths again increase until the Concentrator is turned off for velocities greater than 800 km/s to prevent fractionation

from occurring due to preferential loss of ^{18}O hitting the mirror. In reality, the d/D ratios in Table 2 are upper limits for those experienced in the Concentrator due to the curvature of the mirror and the ion angular distribution (only the energy component normal to the mirror is relevant to the penetration depth), but they show the trends with velocity.

The fractionation trends in Fig. 11 show a general increase in heavy isotope enrichment near the center of the target with increasing ion velocity. This trend is consistent for data points up through 650 km/s, but the pattern changes for 750 km/s as might be expected from the fact that the mirror voltage no longer matches the increased velocity. The 750 km/s data show higher enrichment within 5 mm of the center of the target (only the bottom end of the error bar is visible in the figure), but fractionation at larger target radii is lower than the 650 km/s case. This reflects the change in interplay between the reduced acceleration grid effect and the effects of the deviations from a perfect parabolic shape of the domed grid. The relatively high fractionation at the target center for high-speed wind suggests the possibility of significantly reducing the fractionation gradient by turning the Concentrator off during high-speed streams. However, final calibration of the instrument is planned to use a comparison of neon isotopes in passive collectors with neon in the Concentrator target. If the Concentrator is not operating over the same time period as the passive collectors, this comparison will not be valid. It is not possible to close the passive collectors during high-speed streams. For this reason, the Concentrator is planned to be operated continuously during the time the passive collectors are exposed. The exception is for streams over 800 km/s, which should occur no more than ~1% of the time, and for which the Concentrator cannot function appropriately.

Fig. 12 shows the velocity-weighted average of the fractionation curves, using the velocity distribution from Fig. 2 as a weighting function. The differences between SiC and diamond are due only to differences in backscattering at the target. The fractionation gradients for both diamond and SiC targets are relatively gentle, with the curves staying close to zero permil, as expected from the fact that data points for low-speed wind, which comprise the bulk of ecliptic solar wind, were relatively flat and near unity in Fig. 11. The velocity-weighted curves show heavy isotope enrichments both at the center of the target and at its edges. The center enrichment is due to contributions from high-speed solar wind, while the perimeter enrichment is due to low-speed solar wind. While the nominal values for the two target materials cross at the outer edge, they are well within uncertainty of each other. The error bars in Fig. 12 reflect 1-sigma statistical uncertainties from the numerical simulation, and do not include uncertainties such as those in the velocity distribution. Velocity distributions are known to change over the various portions of the solar cycle, and these will in fact affect the actual fractionation curves on the Concentrator target. Because the Genesis mission will be recording the velocity distribution during flight, a new weighted average based on actual flight data can be compiled upon conclusion of solar wind collection.

Besides radial distributions, azimuthal distributions were also studied to ensure uniformity as a function of azimuthal angle on the target. A series of runs at the 450 km/s setting were compiled totaling 8 million ions. Symmetries on the target were checked which corresponded to symmetry patterns in the instrument. For example, the support ribs from the H rejection grid are known to impart an azimuthal velocity component to ions approaching very close to the ribs. But while flat-grid ribs were observed to result in a 0.1% reduction in fluence to ions in the target regions

corresponding to within ±15 degrees of the ribs, no fractionation was observed. Overall, symmetries corresponding to flat grid support ribs, flat grid insulators, and domed grid dimples were analyzed. A slight fractionation was observed in the case of the domed grid dimple symmetry, but the maximum fractionation was not statistically significant beyond the 1-sigma level (at ~1 permil), relative to the target-wide mean fractionation factor.

As described in Section 3.4, a branch of the ion-flying code was built which imparted thermal distributions in the parallel direction to the ions. Ions of 1 keV/amu (440 km/s) were flown with the appropriate mirror and rejection grid potentials. The results are shown in Fig. 13. This modeling was done at an earlier stage, when the acceleration potential was set to 8 kV instead of the flight value of 6.5 kV. As a result, the fractionation gradients as a function of radius reported here are somewhat larger than those expected for actual operation due to the stronger acceleration grid fractionation effect. No strong differences are seen with thermal Mach numbers. There is a slight trend towards higher fractionation gradients with lower thermal Mach numbers, but it is not clear-cut. Intuitively it would seem that lower thermal Mach numbers would have smaller fractionation gradients due to the smearing implied by low thermal Mach numbers. However, at least in this simulation, the smearing is on a smaller scale than the gradients seen on the target. The actual setting of the rejection grid may play more of a role than the Mach number itself. For example, there is a big operational difference between the M= 5.5 data point (Rejection grid turned to 0 at M<6) and the M=6.5 data (R of 1.0, e.g., Rejection grid set to match the proton peak energy exactly). This may explain the significant differences at either end of the plot for these two settings. At any rate, the vast majority of the flow has thermal Mach numbers > 11 (Fig. 4), for which the rejection grid voltage to E_p ratio, R, is held constant.

Because target materials will be subdivided prior to analysis, is important not only to understand the average fractionation factor for the target as a whole, but also to understand expected fractionation factors for portions of the target. This places constraints on the fractionation gradient from center to edge. For example, if cutting tolerances for sample subdividing are on the order of 100 μm, the uncertainty this produces in the predicted fractionation should still be under ±1 permil. Looking at the curves in Fig. 12, the steepest gradient is just over 1 permil/mm/amu. A cutting uncertainty of ~100 μm should therefore introduce not more than about a tenth of a permil uncertainty in a predicted isotopic composition for a given subdivided sample.

Another important issue is the possibility of diffusion of ions once they are collected in the target. A special effort was made to use low-diffusivity materials in the Concentrator target (cf. Jurewicz et al., 2002) because of the relatively high temperatures it experiences (requirement of < 250 deg C). As a result, no diffusion is expected for oxygen or helium in these materials, while diffusion of H is expected for SiC, but not for diamond.

6. Final Remarks

We have described here the performance of the unique solar-wind Concentrator with respect to oxygen isotopes, helium, and hydrogen. A great effort was made to simulate the instrument and solar-wind parameters as realistically as feasible. While these simulations were the best way of estimating the Concentrator's performance under actual solar wind conditions, the final proof of the instrumental fractionation and concentration factors is expected to be determined by comparisons of neon isotopes in the Concentrator target (and target support) with neon in passive solar wind collectors. Because of the high sensitivity of noble gas mass spectrometry, and the relative proximity to oxygen in the periodic table, neon makes an ideal comparison.

The Concentrator should be very useful for a number of other elements in the solar wind in addition to oxygen. Among these are Li, Be, B, and F which are particularly benefited due to their very low solar-wind abundances and relatively high interest for solar physics purposes (e.g., Burnett et al., 2002). The Concentrator is a back-up collector for nitrogen, in that if passive collection fails to yield an accurate isotopic ratio, Concentrator targets can also be used. The utility of the Concentrator for elements heavier than neon depends on the charge state distributions of these elements. In general, elements through silicon should be efficiently concentrated, but above that, lower-charge ions will begin to be lost, culminating in an average concentration factor of less than ten for iron.

As of this writing (May, 2002) the Concentrator has been in operation for nearly six months. During instrument turn-on it was discovered that the rejection grid was not able to reach full voltage for unknown reasons. A software limit was initially set at 1500 V, but it was later discovered that by limiting voltage increments, potentials of 1880 and eventually 2080 V could be reached. A software patch to limit voltage increments in the 1500+ V range was implemented to take advantage of the increased voltage capability. At nominal solar-wind velocities the rejection grid operates around 1000 V, and is not affected by this limitation. It is only in the relatively small fraction of time that high-speed streams are encountered that the voltage becomes limited by software at these levels. A calculation of the mean proton rejection over the course of the collection period yielded 86% rejection, predicting approximately twice the originally expected hydrogen fluence. One possibility is to turn the Concentrator to non-collection mode for high-speed streams. However, tests to date suggest that the increased hydrogen fluence will not result in any diffusive loss of oxygen from the target materials, though diamond targets may be near the limit of hydrogen fluence without diffusive losses. The desire to obtain concentrated and passive samples of the exact same solar wind has led the team to continue collection over all solar wind speeds < 800 km/s, as originally planned. Thus, with the exception of slightly higher proton fluences, the collection is proceeding as planned.
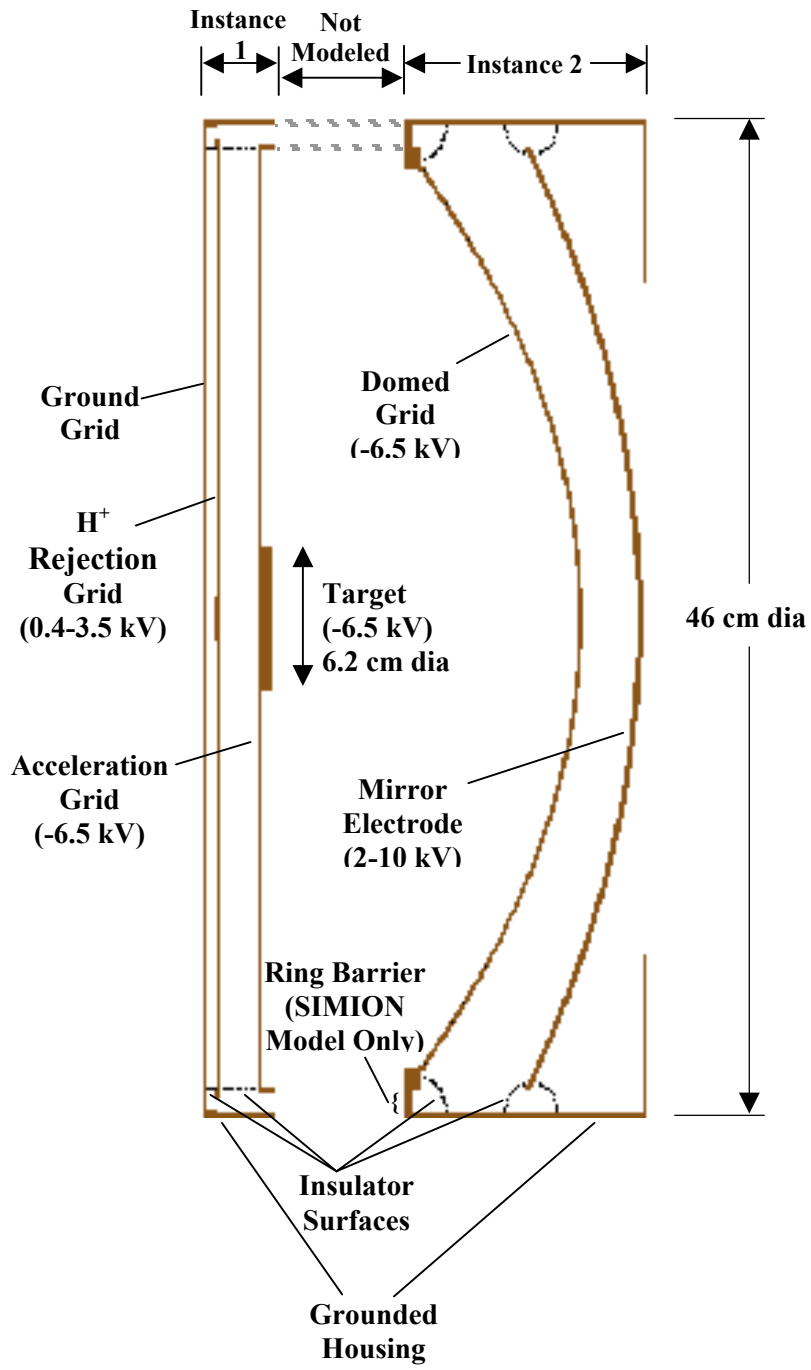
7.0   References

Barraclough, B. L., Dors, E. E., Abeyta, R. A., Alexander, J. F., Ameduri, F. P., Baldonado, J. R., Bame S. J., Casey P. J., Dirks, G., Everett D. T., Gosling, J. T., Grace, K. M., Guerrero, D. R., Kolar, J. D., Kroesche, J., Lockhart, W., McComas, D. J., Mietz, D. E., Roese, J., Sanders, J., Steinberg, J. T., Tokar, R. L., Urdiales, C., and Wiens, R. C.: 2002, 'The Plasma Ion and Electron Instruments for the Genesis Mission', *Spa. Sci. Rev.*, submitted for this issue.

Burnett, D. S., Barraclough, B. L., Bennett, R., Neugebauer, M., Oldham, L. P., Sasaki, C. N., Sevilla, D., Smith, N., Stansbery, E., Sweetnam, D., and Wiens, R. C.: 2002, 'The Genesis Discovery Mission: Return of solar matter to Earth', *Spa. Sci. Rev.,* submitted for this issue.

Ghielmetti, A.G., Balsiger, H., Baenninger, R., Eberhardt, P., Geiss, J., and Young, D.T.: 1983, 'Calibration system for satellite and rocket-borne ion mass spectrometers in the energy range from 5 eV/charge to 10 keV/charge', *Rev. Sci. Instrum.* **54**, 425-436.

Geiss, J., Ogilvie, K.W., von Steiger, R., Mall, U., Gloeckler, G., Galvin, A.B., Ipavich, F., Wilken, B., and Gliem, F.: 1992, 'Ions with low charges in the solar wind as measured by SWICS on board Ulysses', *Solar Wind Seven* (E. Marsch and R. Schwenn, eds.), pp. 341-348, Pergamon Press, Oxford.

Jurewicz, A. J. G., Burnett, D. S., Wiens, R. C., Friedmann, T. A., Hays, C. C., Hohlfelder, R. J., Nishiizumi, K., Stone, J. A., Woolum, D. S., Becker, R., Butterworth, A. L., Campbell, A. J., Ebihara, M., Franchi, I. A., Heber, V., Hohenberg, C. M., Humayun, M., McKeegan, K. D., McNamara, K., Meshik, A., Pepin, R. O., Schlutter, D., and Wieler, R.: 2002, 'Overview of the Genesis solar-wind collector materials, *Spa. Sci. Rev.*, submitted for this issue.

Nahar, S.N.: 1999, 'Electron-ion recombination rate coefficients, photoionization cross sections, and ionization fraction for astrophysically abundant elements. II: Oxygen ions', *Astrophys. J. Suppl.* **120**, 131.

Nordholt, J. E., Wiens, R. C., Abeyta, R. A., Baldonado, J. R., Burnett, D. S., Casey, P., Everett, D. T., Kroesche, J., Lockhart, W., McComas, D. J., Mietz, D. E., MacNeal, P., Mireles, V., Moses, R. W. Jr., Neugebauer, M., Poths, J., Reisenfeld, D. B., Storms, S. A., and Urdiales, C.: 2002, 'The Genesis Solar Wind Concentrator, *Spa. Sci. Rev.*, submitted to this issue.

Summers, H.P.: 1972, 'The density dependent ionization balance of carbon, oxygen, and neon in the solar atmosphere', *Mon. Not. R. Astr. Soc.* **158**, 255.

Wiens, R. C., Huss, G. R., and Burnett, D. S.: 1999, 'The solar oxygen-isotopic composition: Predictions and implications for solar nebula processes', *Met. Planet. Sci.* **34**, 99.

Wimmer-Schweingruber R. F., Von Steiger R., Geiss J., Gloeckler G., Ipavich F. M., and Wilken B.: 1998, 'O^{+5} in high speed solar wind streams: SWICS/Ulysses results', *Spa. Sci. Rev.* **85**, 387-396.

Table 1. Average oxygen charge state distribution used in the Concentrator simulations.

Charge State	Initial Modeling	< 400 km/s	400-500 km/s	500-600 km/s	600-700 km/s	700-800 km/s
+5	0.01	0.004	0.004	0.0040	0.0045	0.0050
+6	0.67	0.641	0.727	0.8017	0.8360	0.9739
+7	0.24	0.292	0.229	0.1785	0.1550	0.0210
+8	0.08	0.063	0.040	0.0158	0.0045	0.0001
Total	1.00	1.00	1.00	1.00	1.00	1.00
Data Source:	Geiss et al., 1992	ACE N = 6571	ACE N = 6997	ACE N = 3000	ACE N = 974	Ulysses N = 26006

Table 2. Ion penetration depths d, relative to the total grid-to-electrode gap D, for ^{16}O ions of different velocities and charge states (q) normally incident on a flat (planar) ion mirror. These represent upper limits for penetration depths in the Concentrator mirror because of the mirror curvature and ion angular distribution.

q	(d/D) @ 350 km/s	(d/D) @ 450 km/s	(d/D) @ 550 km/s	(d/D) @ 650 km/s	(d/D) @ 750 km/s
+5	0.92	0.89	0.87	0.85	0.96
+6	0.89	0.84	0.80	0.77	0.87
+7	0.86	0.81	0.76	0.72	0.80
+8	0.84	0.78	0.73	0.68	0.75

Instance 1

Not Modeled

Instance 2

Ground Grid

H^+ Rejection Grid (0.4-3.5 kV)

Domed Grid (-6.5 kV)

Target (-6.5 kV) 6.2 cm dia

46 cm dia

Acceleration Grid (-6.5 kV)

Mirror Electrode (2-10 kV)

Ring Barrier (SIMION Model Only)

Insulator Surfaces

Grounded Housing
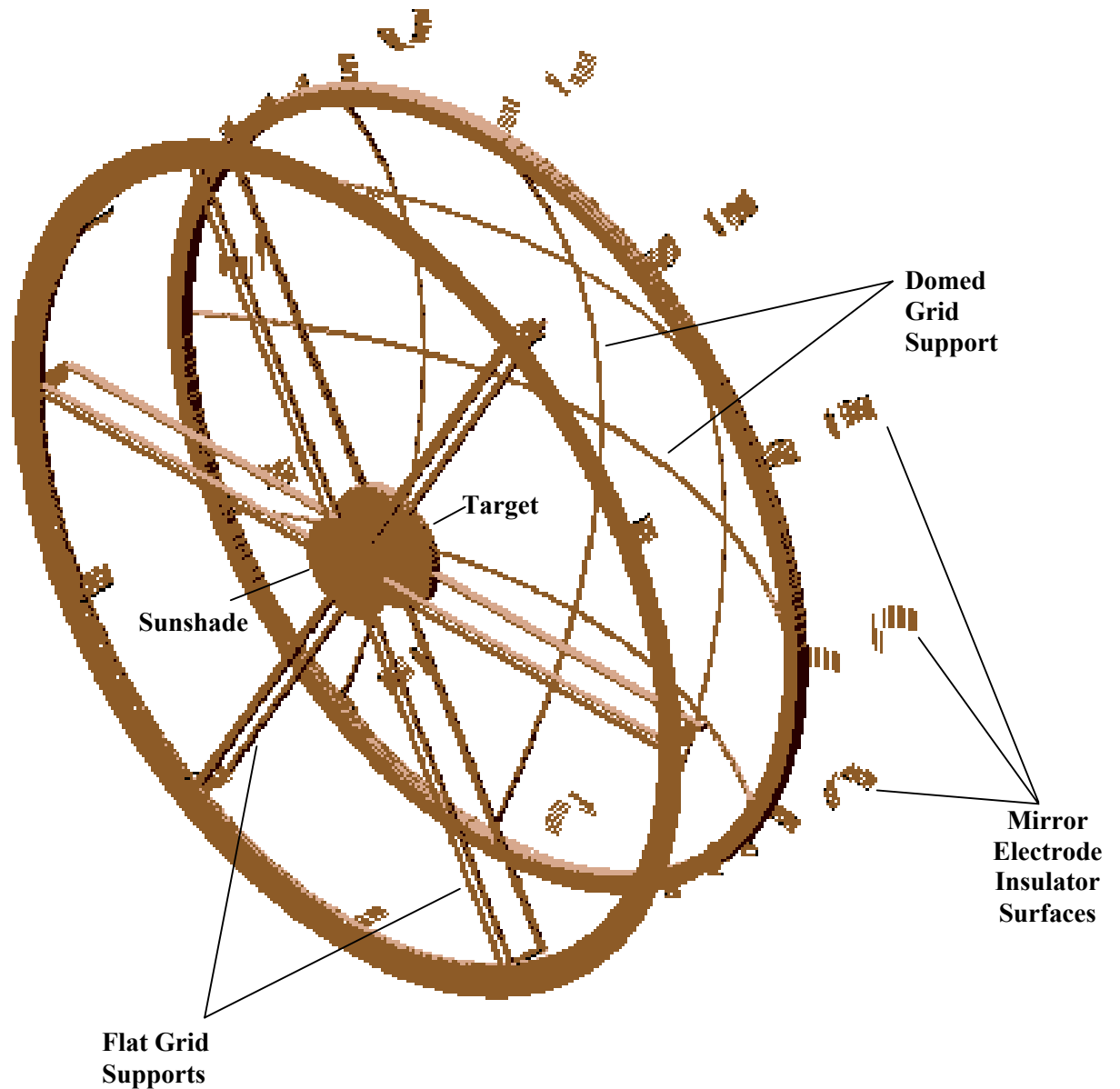
Fig. 1.   SIMION software model of the solar-wind concentrator.   (a) Cross section through the axis of the instrument. (b) Isometric view with housing, grids, and mirror electrode removed to show grid supports, target, sunshade, and insulators.   The 3-D model uses an array of 23 million points. Array point spacing is 0.67 mm. The field-free region between Instance 1 (flat grids and target) and Instance 2 (domed grid and mirror electrode) does not need to be modeled. Compare with Figs. 2 and 3 of Nordholt *et al.* (2002).
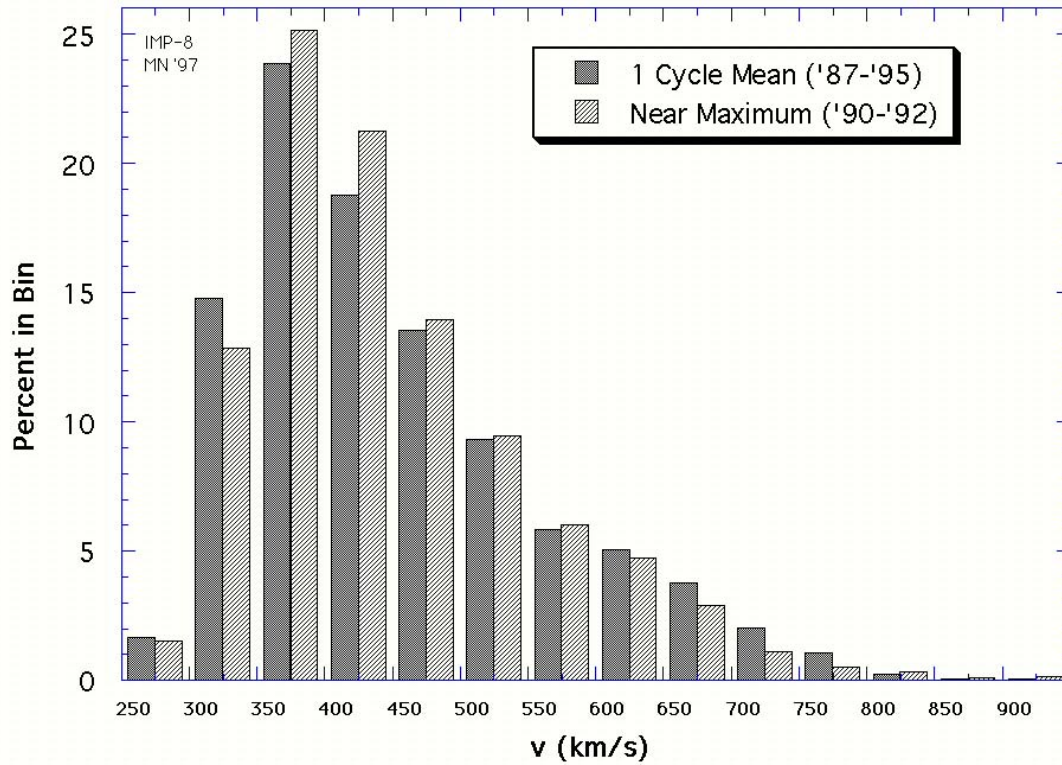
Fig. 2. Proton bulk flow velocity distribution. Results were taken from the OMNI data-base of hourly averages. A companion histogram shows the distribution during an active phase of the solar cycle which roughly matches the period of Genesis observations.
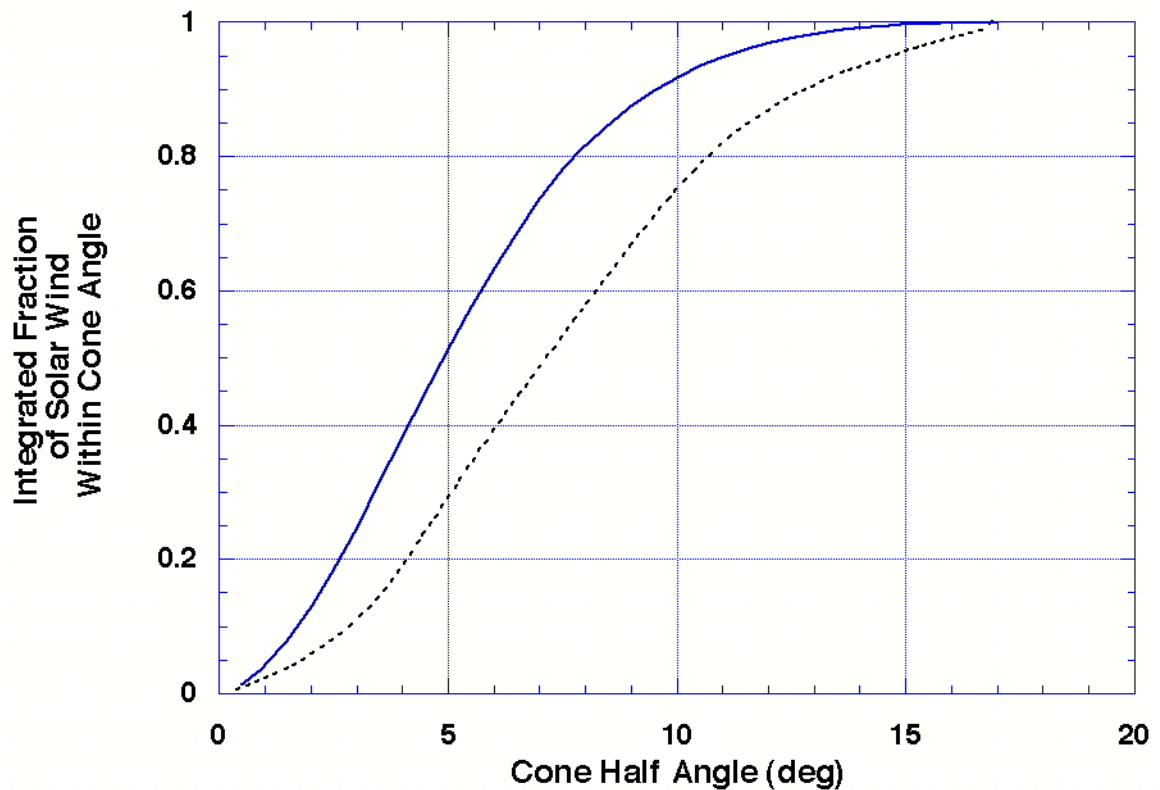
Fig. 3. Calculated angular distribution of ions entering the concentrator (solid line). The calculation takes into account thermal angles relative to bulk flow, bulk flow angle, spacecraft and solar wind vectors, and spacecraft orientation, wobble, and nutation. The curve gives the integrated fraction of the solar wind within a given cone half-angle as a long-term average. The dashed line gives the effective angular distribution for protons when grid scattering is considered for the case of 1.2 kV protons with a rejection grid voltage of 1.15 kV. Angular scattering near grid wires is an insignificant effect for heavy ions, but is clearly significant for protons.

Fig 3
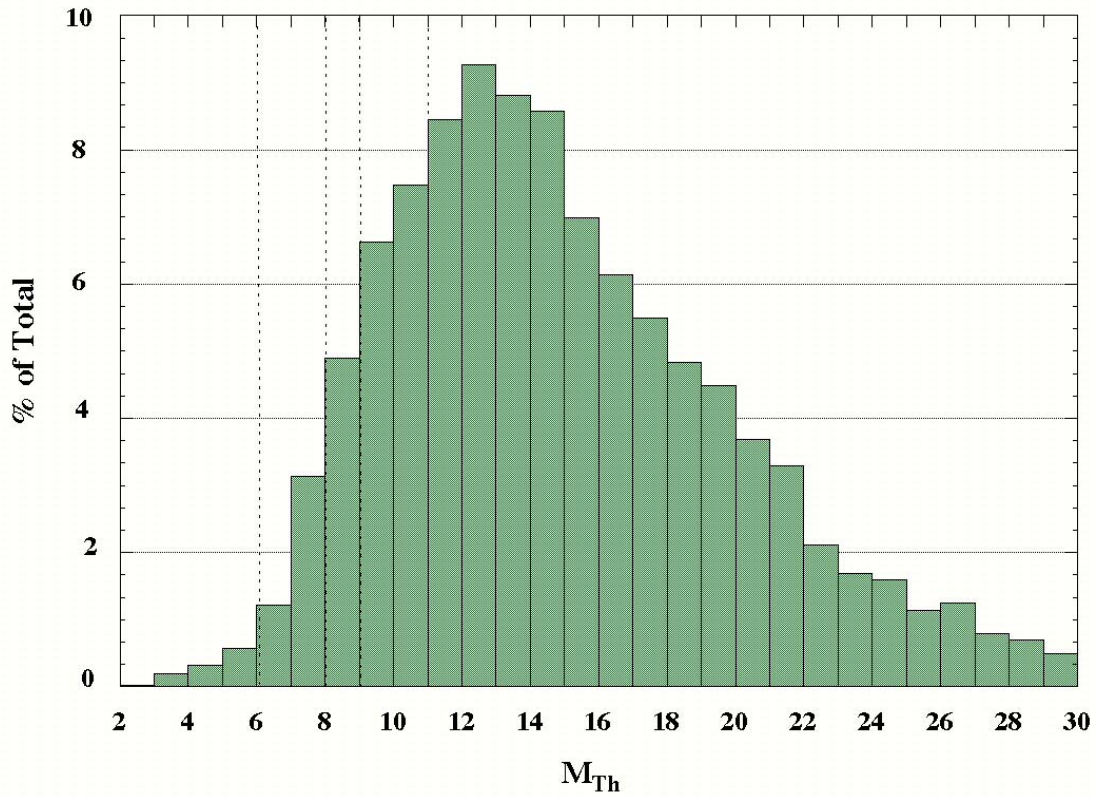
Fig. 4. Histogram of hourly averages of thermal Mach numbers from the OMNI database for 1991-2. Mach numbers greater than 30 are not shown. Vertical dashed lines indicate Mach values at which the concentrator rejection grid changes voltage-to-proton-energy ratios to optimize H rejection while minimizing heavy ion mass fractionation (cf. Nordholt *et al.*, 2002).
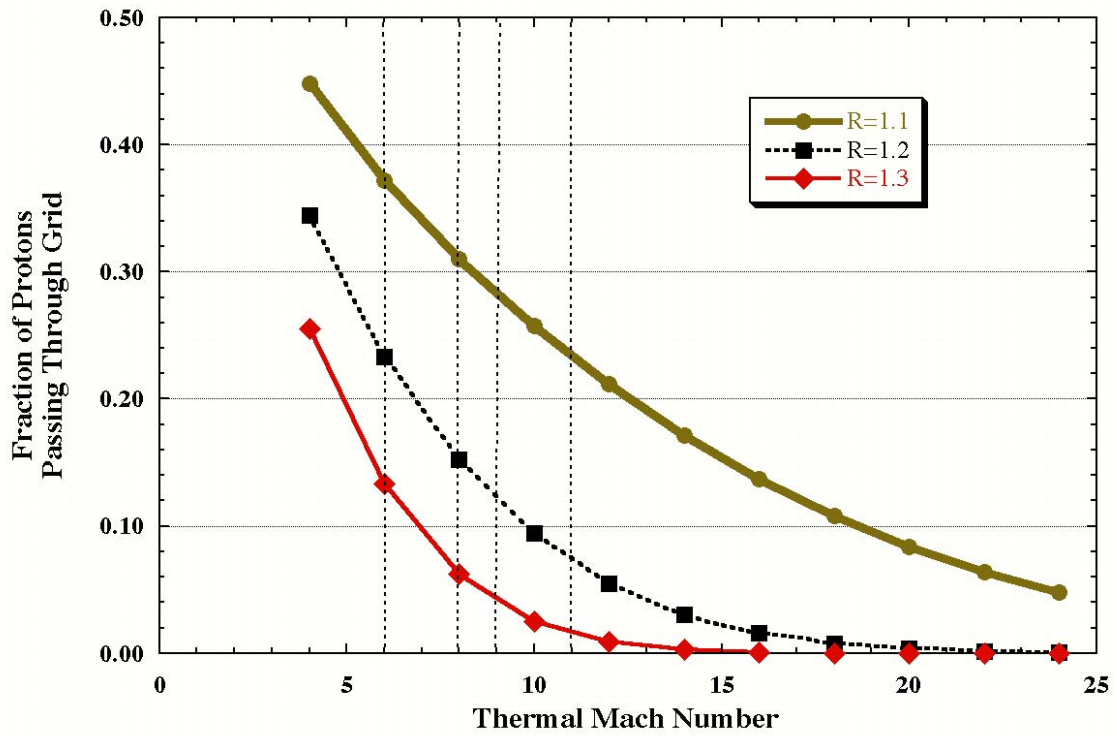
Fig. 5. Fraction of hydrogen passing through the rejection grid as a function of thermal Mach number for voltage to proton-energy ratios of 1.1, 1.2, and 1.3. The Mach number data in Fig. 4 combined with the results in this figure and the voltage to proton-energy ratios given in Nordholt et al. (2002) Table 4 predict a proton rejection of 93.8% on average.
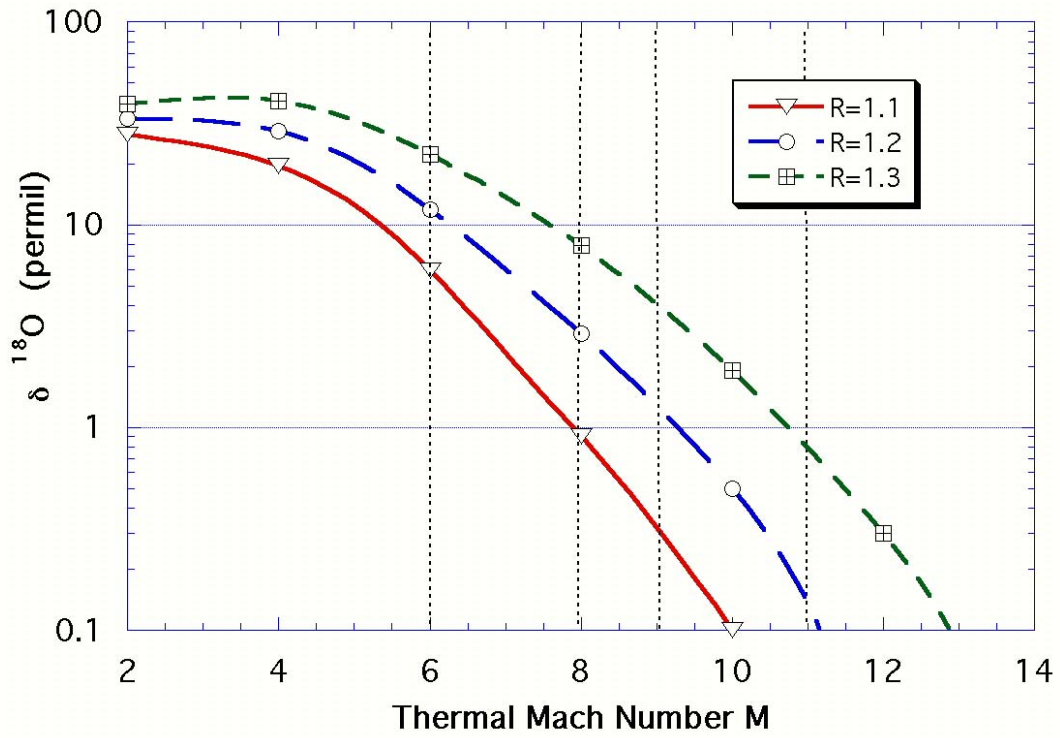
Fig. 6. Calculated mass fractionation of O^{+8} by the rejection grid as a function of thermal Mach number for three different ratios of voltage to E_p used in operation. [$\delta^{18}O$ is the fractionation of the $^{18}O/^{16}O$ ratio in permil, or parts per thousand].
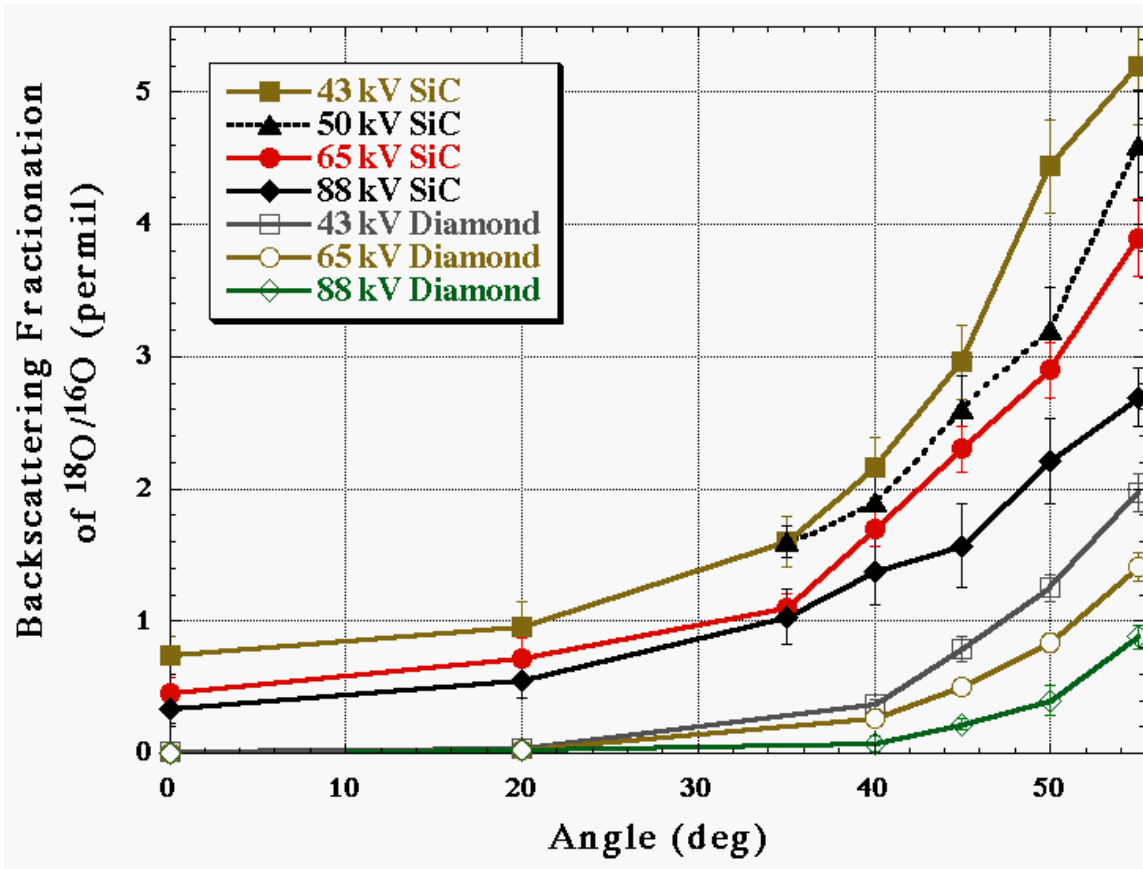
Fig. 7. Backscattering mass fractionation of oxygen isotopes on SiC and diamond targets for typical concentrator energies, as estimated by TRIM. Data points are shown with lines connecting them. The angles with respect to the target depend on the location of the ion when it exits the mirror portion of the concentrator. See text for explanation.
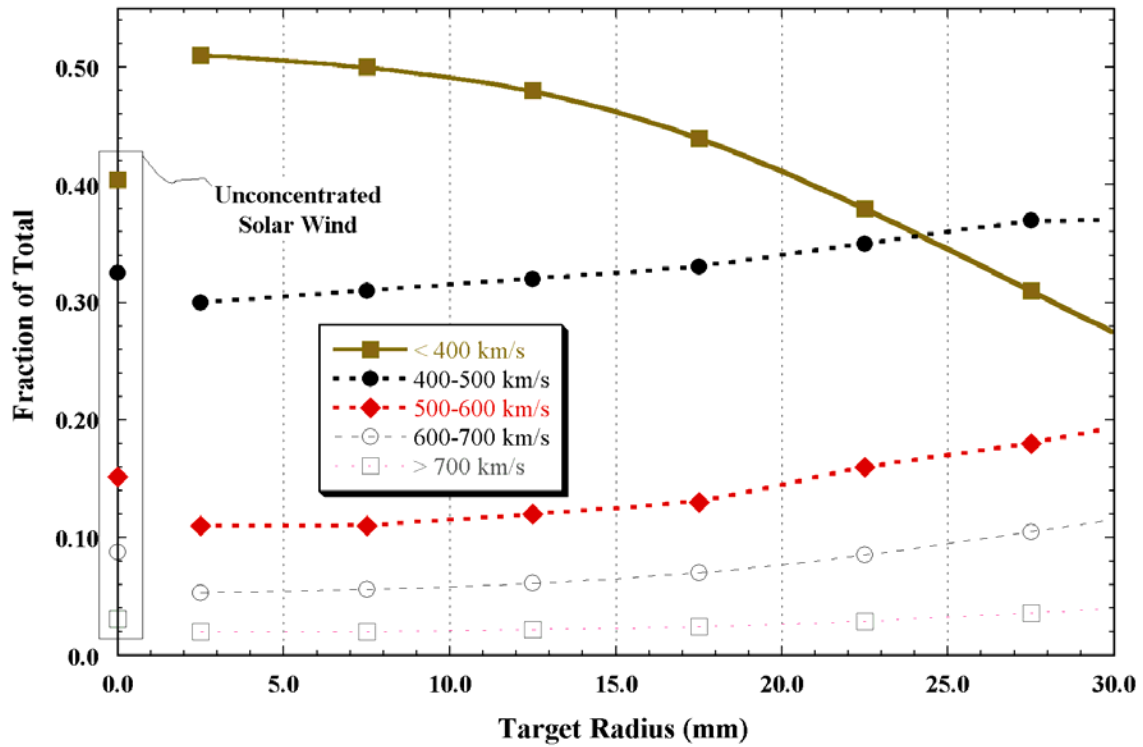
Fig. 8. Relative contributions of solar wind of different velocities to the total fluence at a given target radius. The relative contributions of different velocity solar wind, from Fig. 2, are shown in the box along the y-axis. The relative contributions at each 5 mm radial bin on the target are shown by data points connected by smoothed-fit curves. Low-speed solar wind represents a disproportionate fraction of the ions collected near the center, while high-speed wind is more strongly represented near the outer edge of the target.
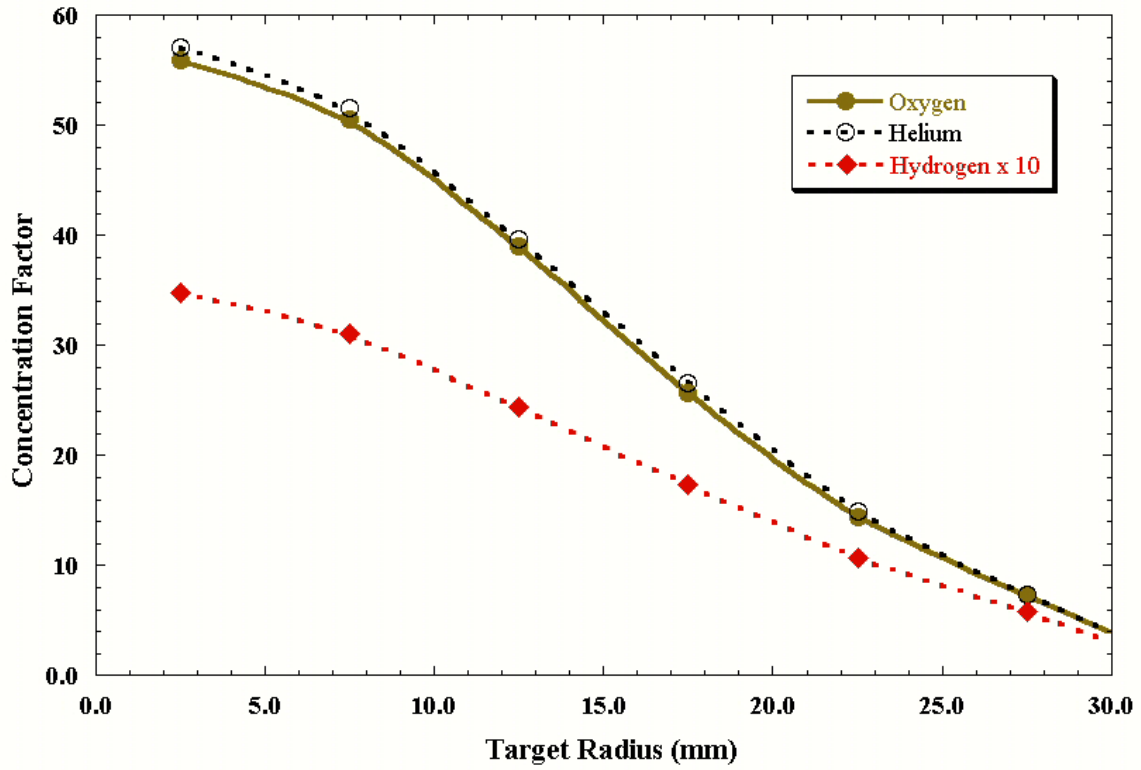
Fig. 9. Concentration factor as a function of target radius for ^{16}O, ^{4}He, and H. Data points are averages for 5 mm radial bins. The curves are smoothed fits to the data points. Concentration factors for protons (magnified in this figure by a factor of 10) are low due to the H Rejection Grid, which removes 93% of the protons to minimize radiation damage to the target.
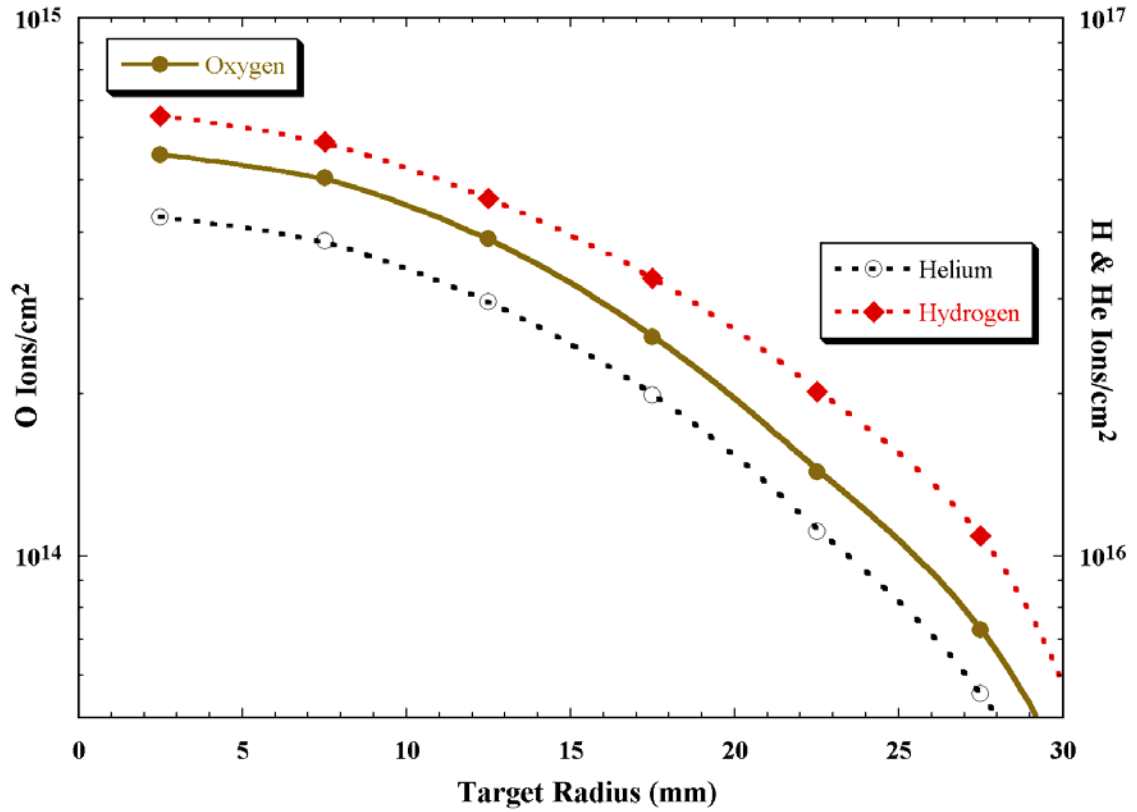
Fig. 10. Predicted target ion densities for ^{16}O, ^{4}He, and H, based on a 2-year exposure time. The oxygen curve corresponds to the left-hand y-axis, while the He and H curves correspond to the right-hand y-axis.
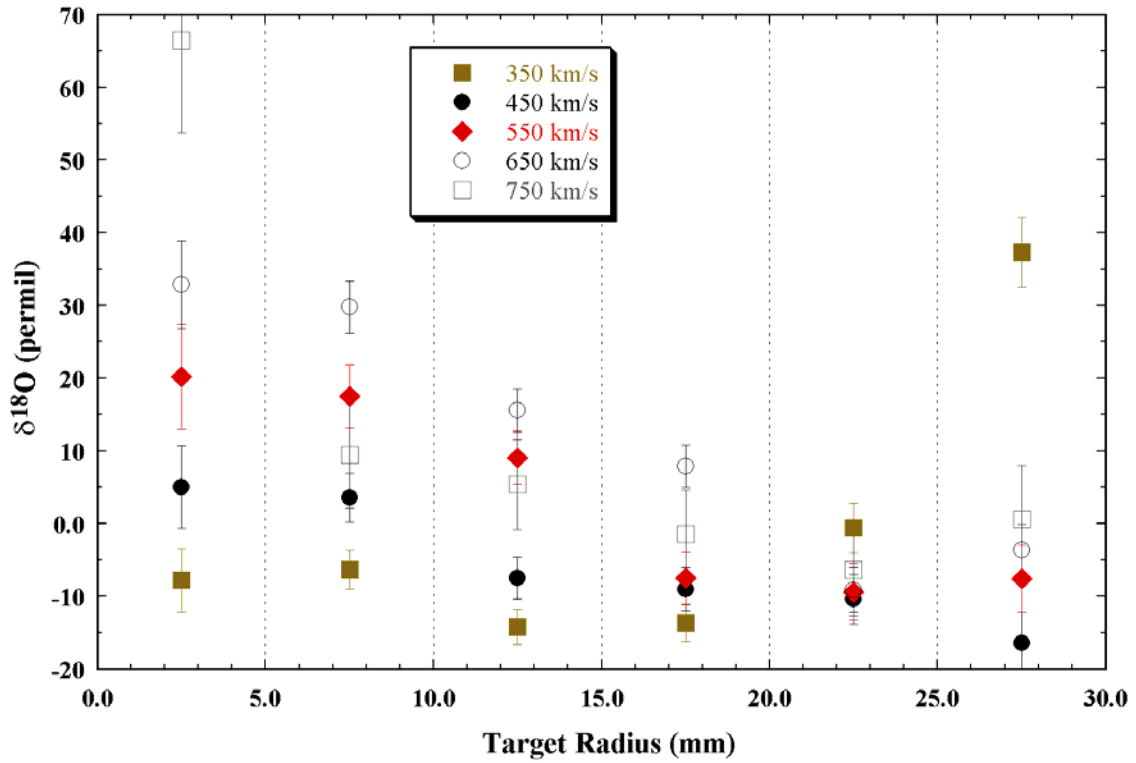
Fig. 11. Instrumental fractionation for solar wind oxygen as a function of target radius for different solar wind velocity ranges for diamond target material. The design was optimized for the mean solar wind velocity of ~440 km/s, with the result that the lower velocities have relatively flat trends.
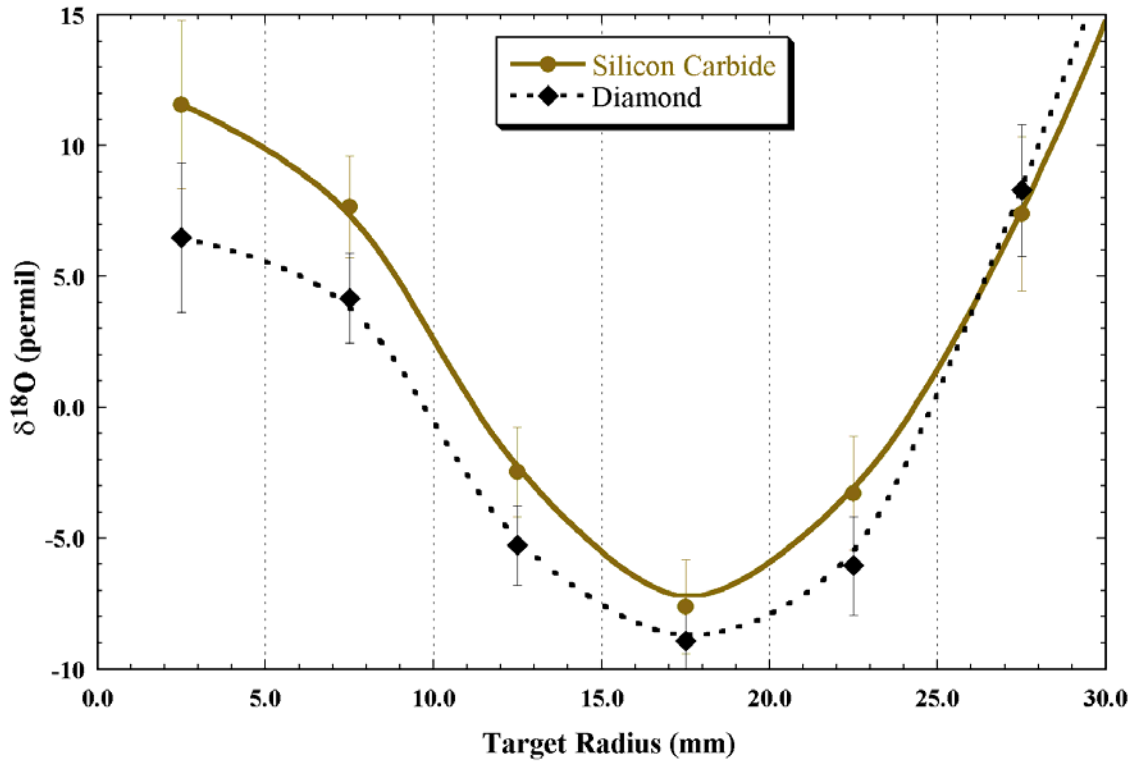
Fig. 12.   Calculated instrumental fractionation for solar wind oxygen as a function of target radius. This result is a weighted average of runs at different solar wind velocities (e.g., from Fig. 11 for diamond). Differences between SiC and diamond target materials are due only to backscattering at the target.
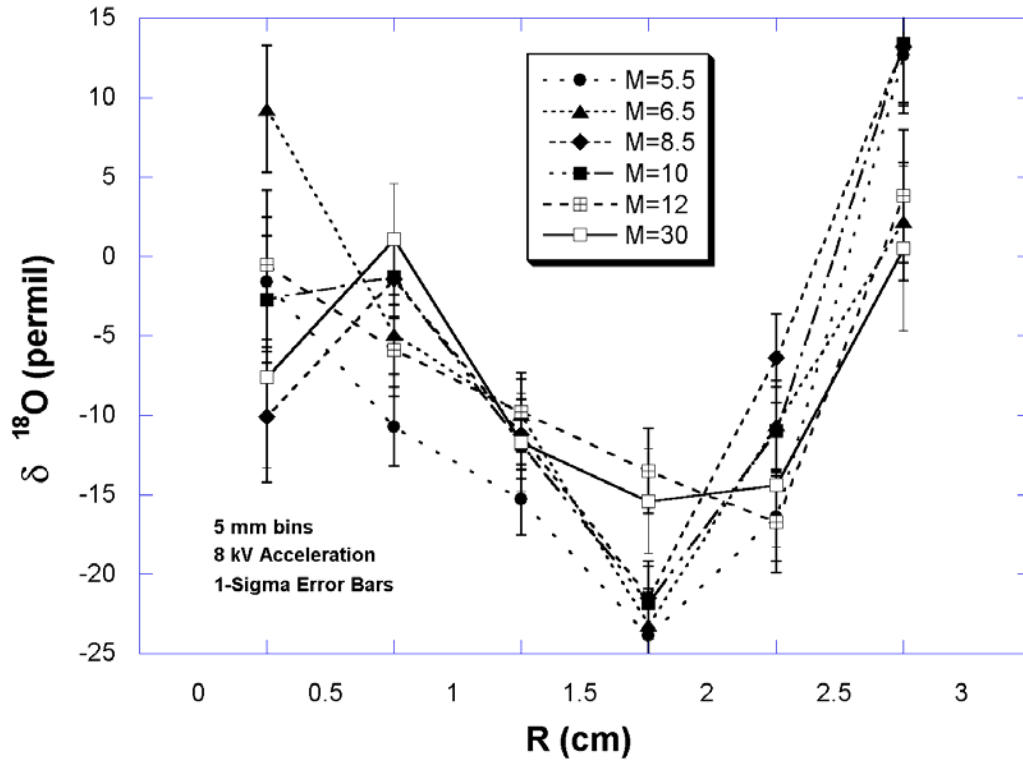
Fig. 13. Instrumental fractionation patterns as a function of target radius for different thermal Mach numbers. These are for 1 keV/amu (440 km/s) ions, with energy distributions only in the parallel direction. The lines simply connect the data points to guide the eye. No significant variations are seen between Mach numbers.